Energy deposition on nuclear emulsion by slow recoil ions for directional dark matter searches

Akira Hitachi[*]
Waseda Research Institute for Science and Engineering, Waseda University, Shinjuku, Tokyo 169-8555, Japan

A. Mozumder
Radiation Laboratory, University of Notre Dame, Notre Dame, Indiana 46556-5674, USA

Kiseki D. Nakamura[†]
High energy physics group, Tohoku University, Sendai, Miyagi 980-8578, Japan

(Received 23 May 2019; revised 21 December 2021; accepted 20 January 2022; published 22 March 2022)

The electronic energy deposited on nuclear emulsions by C ions of 5–200 keV and Kr ions of 5–600 keV is evaluated and compared with those deposited by fast ions for designing and fabricating fine-grain nuclear emulsions for directional dark matter searches. The nuclear quenching factor and the electronic linear energy transfer, which refers to the specific electronic energy deposited along the ion track, are evaluated. The so-called core and penumbra of heavy-ion track structure is modified to understand the track caused by recoil ions produced by dark matter candidate, i.e., weakly interacting massive particles, striking a nucleus in the AgBr crystal of nuclear emulsion. Very heavy recoil ions, 100–180 keV Pb ions, produced in α decay are also studied. Furthermore, the track structures due to protons of 25–80 keV are evaluated to consider the influence of background neutrons in underground laboratories.

DOI: 10.1103/PhysRevD.105.063014

I. INTRODUCTION

Identification of dark matter is one of the most compelling challenges in cosmology, astrophysics, and particle physics. Scientific evidences, such as the rotational velocity of galaxies in clusters [1], rotational velocity of stars and gases in galaxies [2,3], and the gravitational lensing [4–6], confirm the existence of nonbaryonic dark matter. Dark matter consists a quarter of the Universe's energy. The Galaxy is surrounded by dark matter. The solar system travels around the galactic center at 230 km/s towards Cygnus. The detection of weakly interacting massive particles (WIMPs), which are the leading candidates for galactic dark matter, usually involves ionization, excitation, and chemical reactions induced by recoil ions with energies of a few to a few tens of keV, produced by the elastic scattering of WIMPs [7–11]. Currently, various types of detectors are observing two or more types of signals and exploiting the difference in the response for slow recoil ions and background γ rays [12–14]. The kinetic spectrum of recoil ions can be described as similar to exponential, not monochromatic. The directional detection of WIMPs will facilitate the discrimination of nuclear recoil signals from background γ rays, neutrons, and neutrinos, using the daily modulation of WIMP wind [11,15].

Nuclear emulsions have been used for detecting various particles under a wide energy range. Analyzing the details pertaining to the ion track provides information on the type of particle and its energy [16]. The sensitivity of nuclear emulsions to particle and their energies can be adjusted, according to the experimental requirement, by changing the grain size and developing procedure. Most γ rays, which are the major source of backgrounds, can be rejected by adjusting the sensitivity of the nuclear emulsion. Fine grain nuclear emulsions have been proposed and are being developed for the directional detection of WIMPs [17–19]. The fundamental properties of slow ions ($v \lesssim v_0 Z_1^{2/3}$, where v is the velocity of the ion, $v_0 \approx c/137 = 2.2 \times 10^8$ cm/sec is the Bohr velocity, c is the velocity of the light, and Z_1 is the atomic number of the ion) interacting with detector media, such as stopping power, energy sharing, and quenching are important for designing and constructing dark matter detectors. Herein, the electronic energy deposited on nuclear emulsions is discussed to understand ion track images. We propose a model for predicting the footprints of WIMPs in nuclear emulsions. The electronic linear energy transfer (LET) plays an important role in slow ion collisions [10,20–22].

The nuclear emulsion consists of a AgBr crystal (grain) sustained in gelatin [17–19]. Conduction electrons

[*]a.hitachi@kurenai.waseda.jp
[†]kiseki@epx.phys.tohoku.ac.jp

generated by charged particles may become trapped, combine with mobile silver ions, and form aggregates of silver atoms. Latent image specks are formed on each crystal by the following reactions:

$$e^- + Ag^+ \rightarrow Ag, \tag{1}$$

$$e^- + Ag^+ + Ag \rightarrow Ag_2 \cdots Ag_n. \tag{2}$$

Development makes a Ag filament structure. The density and number density of AgBr crystal are 6.473 g/cm^3 and 2×10^{22} cm^{-3}, respectively. The atomic distance a is 2.88 Å. The direct band gap energy E_g is 4.292 eV [23,24] and the average energy W required for an ionization is 5.8 eV [25]. A standard nuclear emulsion have a grain size of 200 nm, whereas fine-grain emulsion shows a grain size of 18–40 nm. The density of fine-grain emulsion is 3.2 g/cm^3, and the mass ratio of the atoms can be approximated as Ag:Br:C(N, O) = 9:7:2. The number density of atoms is 8×10^{22} cm^{-3}. The sensitivity of the nuclear emulsion considerably depends on the grain size and developer.

In this study, we present the results of the calculation of the energy deposition. The model assumptions are clear and simple. When necessary, one can refine the calculation or extend the model. The track structure obtained here does not immediately predict the latent image in the nuclear emulsion because of the complex nature of response of the nuclear emulsion to ionizing radiation. The present results can be employed to adjust the grain size and sensitivity of the nuclear emulsion and determine the optimum development conditions.

II. HEAVY ION TRACK

A simple model is considered to obtain some insights into the response of the nuclear emulsion to ions because the composition, structure, and chemical reactions of nuclear emulsion are considerably complex. Furthermore, obtaining accurate values of some physical and chemical quantities is challenging. Katz and coworkers proposed the δ-ray theory of track structure with respect to the response of nuclear emulsions [26,27], because the "visual" radial images of fast-ion track are largely achieved by the penetration of energetic secondary electrons (δ rays). However, the δ ray theory is unsuitable for slow recoiling ions because the energy and range of δ rays are excessively low. The nuclear emulsion used for detecting WIMPs can be adjusted to be insensitive to electron and sensitive to ions to suppress the background electrons. We propose a model similar to the so-called core and penumbra of heavy-ion track structure. The track of fast ions, such as α particles and ions with energy of several MeV/n to a few GeV/n, can exhibit a cylindrical geometry comprising a high-density core and a surrounding less-dense penumbra [28–30]. Cores are formed via glancing collisions (distant collisions) and penumbras are formed by δ rays produced via knock-on collisions (close collisions). Glancing collisions frequently transfer small amounts of energy within the core, a region with a finite size. The core radius r_c for nonrelativistic ions is given by the Bohr criterion:

$$r_B = \hbar v/2E_1, \tag{3}$$

where $\hbar$ is Plank's constant divided by 2π, v is the velocity of the incident ion, and E_1 is the energy of the lowest electronic excited state of the medium. The stopping power theory supports the equipartition of the total energy loss between the glancing and close collisions. The initial radial distribution of track core produced via the glancing collisions may be approximated as a Gaussian distribution with a size parameter r_c, which is the same as the core radius [31]

$$D_g = \frac{\mathrm{LET}/2}{\pi r_c^2} \exp\left(-r^2/r_c^2\right), \tag{4}$$

where r is the radius and $\mathrm{LET} = -\mathrm{d}E/\mathrm{d}x$.

The knock-on collisions transfer large amount of energy less frequently producing δ rays. The δ rays deposit some of their energy in the core and the remaining in the surrounding penumbra. The contributions of δ ray to the core and penumbra are expressed using a simple model [29,30],

$$D_k = \frac{\mathrm{LET}/2}{2\pi r_c^2 \ln\left(\sqrt{e} r_p/r_c\right)}, \qquad r \le r_c, \tag{5}$$

$$D_k = \frac{\mathrm{LET}/2}{2\pi r^2 \ln\left(\sqrt{e} r_p/r_c\right)}, \qquad r_c < r \le r_p, \tag{6}$$

where r_p is the radius of the penumbra and is obtained by the range of the δ rays of the maximum energy. A normal ejection of δ rays with a constant energy loss is assumed. The kinematically limited maximum δ-ray energy is expressed as $4Em_e/M$ (where m_e is the electron mass and M is the mass of incident particles), or in the case of relativistic ions, $2m_e c^2\beta^2/(1-\beta^2)$ (where $\beta = v/c$). A typical initial radial distribution of a dose in the AgBr crystal by 10 MeV proton is shown in Fig. 1. The direct energy gap E_g is adopted as E_1.

The conventionally employed simple model [29] assumes a constant dose due to glancing collisions, instead of the model expressed in Eq. (4):

$$D_g = \frac{\mathrm{LET}/2}{\pi r_c^2}, \qquad r \le r_c. \tag{7}$$

Thus, the dose within the core is the sum of Eqs. (5) and (7) (Fig. 1). The sharp distinction between the core and penumbra in the model is an artificial concept primarily introduced to facilitate the analytical process [29].

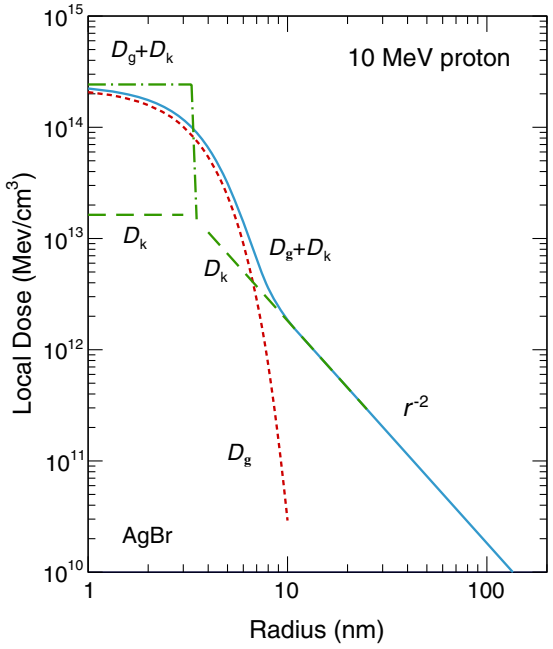

FIG. 1. The core and penumbra structure of heavy-ion track shown for 10 MeV protons in AgBr crystal. The solid and dotted curves show the present model. Dashed and dot-dashed lines show the conventionally employed model [29,30]. Only a part of the penumbra is shown. Suffixes g and $\mathfrak{g}$ indicate glancing collisions, while k indicates knock-on collisions.

By introducing a Gaussian distribution for the glancing collisions, i.e., Eq. (4), the present model achieves a moderate distinction. The Gaussian form can be used to treat redistribution of energy and chemical reactions in track core, such as diffusion reactions involved in scintillation quenching in liquid Ar and Xe [22,31]. The fraction of energy deposited within a cylinder of radius r is expressed as

$$F = \frac{1}{2} + \frac{1}{4\ln(\sqrt{e}r_p/r_c)} + \frac{\ln(r/r_c)}{2\ln(\sqrt{e}r_p/r_c)}, \quad r_c < r \le r_p. \tag{8}$$

The first and second terms on the right side of Eq. (8) represent the contributions of the glancing collisions and δ rays to the core, respectively. The third term is attributed to the δ rays deposited in the penumbra within a radius r. When r is sufficiently greater than r_c, Eq. (8) can be applied for the present model. The track parameter values of various particles are listed in Table I.

For relativistic particles, the radius according to Fermi's theory

$$r_F = \lambda\beta, \tag{9}$$

is used for r_c, where λ is the maximum core size, which is expressed as [33]

$$\lambda = \chi_{max} c/n\omega_0, \tag{10}$$

where, $\chi_{max} = 1.074$ and $n = \epsilon^{1/2}$ is the refractive index, taken to be 2.253 for AgBr crystal. The angular frequency ω_0 in the compound consist of light elements, such as water, the geometrical mean ionization potential of the electrons (excluding the K electrons) is used.

The following form [30],

$$\lambda = c/\omega_p, \tag{11}$$

is often used with the plasma frequency:

TABLE I. Data for various ion tracks in AgBr crystal. The ranges correspond to the projected range in nuclear emulsion [17,32]. The r_c and r_p values are for the initial energy E. The r_c values for the low-energy p, C, Kr, and Pb ions show the expanded core radii, see the text. The data irrelevant to the calculation are not listed and marked "…".

Particles	Energy keV	Range μm	q_{nc} E_η/E	$\langle LET_{el}\rangle$ keV/μm	E_δ^{max} keV	r_c nm	r_p nm
Protons	25	0.29	1.0	87	0.05	0.48[a]	…
Protons	80	0.74	1.0	109	0.18	0.46[a]	1.5
Protons	10×10^3	630	1.0	16	22	3.3	2.1×10^3
Alphas	5.3×10^3	25	1.0	212	2.9	1.2	63
C	3.48×10^6	…	1.0	50[b]	735	11	5.9×10^5
C	30	0.093	0.58	190	…	0.7[a]	…
C	100	0.30	0.77	260	…	0.8[a]	…
Kr	30	0.024	0.27	340	…	0.9[a]	…
Kr	100	0.060	0.33	550	…	1.2[a]	…
Kr	200	0.11	0.38	680	…	1.3[a]	…
Kr	600	0.35	0.47	820	…	1.5[a]	…
Pb	100	0.040	0.14	360	…	1.0[a]	…
Pb	170	0.058	0.19	540	…	1.2[a]	…

[a]Expanded core radius.
[b]Initial LET.

$$\omega_p = \sqrt{\frac{n_e e^2}{m^* \epsilon_0}}, \tag{12}$$

where n_e is the number density of electrons, e is the charge of electron, m^* is the effective mass of the electron, and ϵ_0 is the permittivity of free space. The λ values in water are 93 Å [33] and 103 Å [29], for Eqs. (10) and (12), respectively, and they are close to each other. However, the use of the plasma frequency for heavy elements, such as AgBr, yields a very large $\hbar\omega_0$, consequently, an unreasonably small λ value. Because, AgBr crystal has the band structure, we take the average energy W required for produce a hole-electron pair, yielding $\hbar\omega_0 = 5.8$ eV or that $\omega_0 = 8.81 \times 10^{15}$ sec^{-1}. Then we obtain $\lambda = 170$ Å for AgBr crystal using Eq. (10).

The range of electron below 10 keV energy is unreliable because of experimental difficulties. The Bethe theory becomes invalid in this energy region. However, with respect to the study of track structure, it is important to describe the behavior of δ rays with energy of a few keV. Iskef *et al.* [34] studied and compared published experimental information on the penetration depths of electrons. They provided the following "best fit" expression applicable to all media at energy of 20 eV–10 keV with a simple scaling factor Z/A. The extrapolated ranges R_{ex} (in μg/cm^2) are given by

$$\ln\left[(Z/A)R_{ex}\right] = -4.5467 + 0.31104 \ln E + 0.7773(\ln E)^2, \tag{13}$$

where E is the energy in eV. Because, Z/A values for Ag and Br are practically the same, the R_{ex} values for Ag was calculated and the range in AgBr crystal was obtained using the density of the AgBr crystal.

The track dimensions r_c and r_p depend only on the particle velocity β. D_k decrease with r^{-2} at large r values. The same shape can be applied to various ions exhibiting the same energy per nucleon (MeV/n). However, the dose (energy density) depends on the LET and thus on the particle charge. The LET scales as a square of the effective charge Z_{eff}^2, which is a function of the velocity [30].

III. SLOW RECOIL IONS

A. Stopping powers

For the interaction of slow ions with matter, the nuclear stopping power S_n is of the same order of magnitude as the electronic stopping power S_e [35]. The sum of the two yields the total stopping power S_T: $S_T = S_n + S_e$. For slow ions, the r_c value obtained using the Bohr criterion becomes unreasonably small to make excitation higher than E_1. The projectile cannot get sufficiently close to the target atom owing to the repulsive potential in an ordinary manner. Furthermore, the kinematically limited maximum energy for secondary electrons may not exceed E_1 in some cases. This implies that the usual theories for S_e based on ion-atom collisions, such as Bohr's classical theory and Bethe's quantum mechanical theory, are inapplicable to these slow collisions. Lindhard *et al.* considered the dielectric response [36]. A charged particle incidents on the electron gas induce polarization and alter the dielectric constant. Consequently, the incident particle receives an electric force in the opposite direction that generates S_e. For slow ions, S_e is expressed as $(d\varepsilon/d\rho)_e \approx k\varepsilon^{1/2}$, where ε is the dimensionless energy and ρ is the dimensionless range. Based on the Thomas-Fermi treatment, S_e is given to a first approximation by [37]

$$S_e = \xi_e \times 8\pi N e^2 a_0 \frac{Z_1 Z_2}{(Z_1^{2/3} + Z_2^{2/3})^{3/2}} \frac{v}{v_0}, \quad \text{with} \quad \xi_e \approx Z_1^{1/6}, \tag{14}$$

where Z and A are the atomic number and the atomic mass, respectively, suffixes 1 and 2 indicate the projectile and target, respectively; a_0 is the Bohr radius ($a_0 = \hbar^2/m_e e^2 = 0.529$ Å); and N is the number of stopping atoms per unit volume. The parameter k is obtained by Eq. (14) and expressed as $k = 0.133 Z_2^{2/3} A_2^{-1/2}$ for $Z_1 = Z_2$. For most cases, $k = 0.1$–0.2.

The nuclear process follows the usual procedure of a screened Rutherford scattering. The nuclear stopping power can be expressed analytically using the Firsov potential [38] as follows:

$$S_n = \frac{4\pi N a_{TFF} A_1 Z_1 Z_2 e^2}{A_1 + A_2} \frac{\ln \varepsilon_n}{2\varepsilon_n(1 - \varepsilon_n^C)}, \tag{15}$$

where $C = -1.49$ and a_{TFF} is the Thomas-Fermi-Firsov screening radius,

$$a_{TFF} = 0.8853 a_0/(Z_1^{1/2} + Z_2^{1/2})^{2/3}, \tag{16}$$

and

$$\varepsilon_n = \frac{a_{TFF} A_2}{Z_1 Z_2 e^2 (A_1 + A_2)} E. \tag{17}$$

The stopping powers discussed above yield the same values as those in the Hahn-Meitner Institute (HMI) tables [39] at a low E value.

Lindhard *et al.* [36,37] proposed a slightly different expression for the screening radius a_s:

$$a_s = 0.8853 a_0/(Z_1^{2/3} + Z_2^{2/3})^{1/2}. \tag{18}$$

The energy E is converted to ε as

$$\varepsilon = C_\varepsilon E = \frac{a_s A_2}{Z_1 Z_2 e^2 (A_1 + A_2)} E. \tag{19}$$

For $Z_1 = Z_2$, Eq. (19) becomes $\varepsilon = 11.5 Z_2^{-7/3} E$. C_ε corresponds to E in keV: 0.1759, 0.0350, 0.00268, and 0.00500 for C ions in C, C ions in Kr, Kr ions in C, and Kr ions in Kr, respectively.

The effect of the charge state Q of the projectile on the stopping power is determined by the screening radius [a_{TFF} in Eq. (16) or the corresponding part in Eq. (14)] [40]. The dependence of the stopping power on Q is moderate, as confirmed by replacing Z_1 with $\xi_1 = Z_1 - Q$. The projectiles of various charge states exchange electrons with target atoms and soon achieve charge equilibrium based on the ion velocity. The Q values determined using the charge equilibrium for slow ions are small, indicating that Q affects quite weakly the stopping power. If the different charge states give different results, it is likely as a result of the surface effects.

B. Electronic LET

The electronic stopping power S_e does not directly correspond to the electronic energy deposited on the target matter. The secondary ions repeatedly undergo collision processes. A considerable amounts of energy ν goes to atomic motion, which is wasted as heat in ordinary detectors, after the cascade processes of stopping collisions. Only a part of energy η is utilized for the electronic excitation, which can induce ionization, excitation, and chemical reactions. It is necessary to obtain the ratio, $q_{\mathrm{nc}} = \eta/\varepsilon$ (the nuclear quenching factor or Lindhard factor) to evaluate the detection efficiency, etc. Lindard *et al.* [35] solved the homogeneous integral equation for $\nu(=\varepsilon - \eta)$ and gave numerical results for $Z_1 = Z_2$ for $k = 0.1$, 0.15, and 0.2. The k value for Kr ions in Kr is 0.158; therefore, it can be approximated as $k = 0.15$. The following expressions were obtained from Fig. 3 in Ref. [35]:

$$\eta = 0.2958\varepsilon^{1.1130} + 0.1304\varepsilon^{1.4212}, \qquad \varepsilon \le 2. \tag{20}$$

They also provided a comprehensive formula for ν; $\eta = \varepsilon - \nu$ is expressed as

$$\eta = \frac{k\varepsilon g(\varepsilon)}{1 + k \cdot g(\varepsilon)} \tag{21}$$

for the k values of 0.1–0.2. The comprehensive formula reproduces the numerical ν within an accuracy of several %. The function $g(\varepsilon)$ is later fitted by Lewin and Smith [9] as

$$g(\varepsilon) = 3\varepsilon^{0.15} + 0.7\varepsilon^{0.6} + \varepsilon. \tag{22}$$

Therefore, the nuclear quenching factor for recoil ions in a single element material ($Z_1 = Z_2$) is obtained by interpolation of the numerical results (Figs. 3 and 4 in Ref. [35]) or the asymptotic form using Eqs. (21) and (22) (Fig. 2).

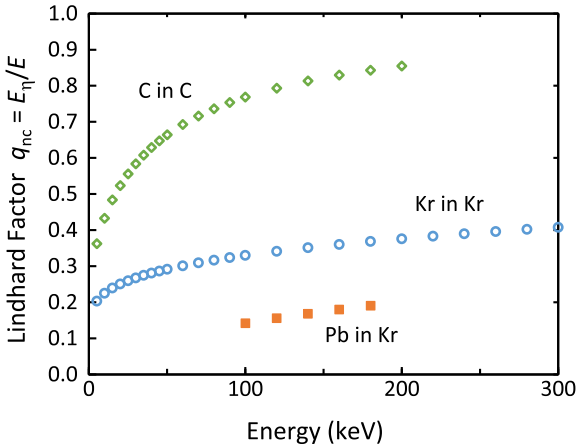

FIG. 2. Lindhard factor ($q_{\mathrm{nc}} = \eta/\varepsilon$) for C ions in C and Kr ions in Kr as a function of energy. The q_{nc} values for Pb ions in Kr are also shown.

The information on microscopic electronic energy deposition is required to evaluate the latent images produced in the nuclear emulsion. The electronic LET ($\mathrm{LET_{el}}$) becomes an important concept in slow ion collisions [20,21]. We have simply $\mathrm{LET_{el}} = -\mathrm{d}(q_{\mathrm{nc}}E)/\mathrm{d}x$. However, a slight complication arises because q_{nc} (or η) is an integrated quantity. Therefore, we achieve

$$\mathrm{LET_{el}} = -\frac{\mathrm{d}E_\eta}{\mathrm{d}x} = -\frac{\mathrm{d}E_\eta}{\mathrm{d}E}\frac{\mathrm{d}E}{\mathrm{d}x} = \frac{\mathrm{d}E_\eta}{\mathrm{d}E} S_{\mathrm{T}}, \approx \frac{\Delta E_\eta}{\Delta E} S_{\mathrm{T}}, \tag{23}$$

where $E_\eta = \eta/C_\varepsilon$. For clarify, an averaged form is employed:

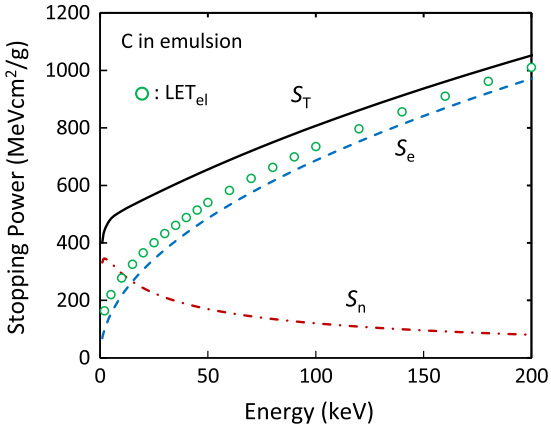

FIG. 3. Stopping powers (S_{T}, S_{n}, S_{e}) and electronic LET [$\mathrm{LET_{el}}$ ($=-\mathrm{d}E_\eta/\mathrm{d}x$)], for C ions in nuclear emulsion as a function of energy. $\mathrm{LET_{el}}$ is obtained using the q_{nc} values for C ions in C (see the text).

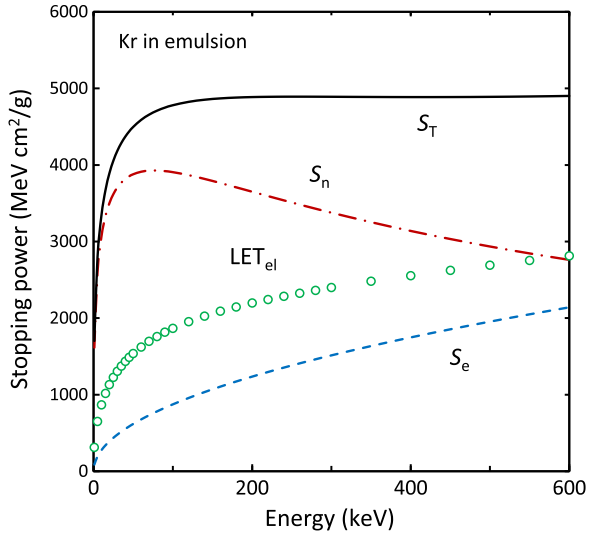

FIG. 4. Stopping powers (S_T, S_n, S_e) and electronic LET [LET_{el} ($=-dE_\eta/dx$)] for Kr ions in nuclear emulsion as a function of energy.

$$\langle LET_{el}\rangle = E_\eta/R = q_{nc}E/R, \tag{24}$$

where R is the range. The electronic LET represents the specific electronic energy deposited along the ion track, and is not the same as the electronic stopping power S_e (Figs. 3 and 4). LET_{el} is greater than S_e for slow ions because secondary ions can donate energy to promote the electronic excitation when their energy is large enough. For fast ions, the contributions from nuclear scattering are negligible. Therefore, LET and LET_{el} are the same.

C. Slow recoil ion track

The track structure for slow recoil ions is different from the aforementioned core and penumbra of the heavy-ion track structure. We assume that most δ rays produced by recoil ions do not have sufficient energy to effectively escape the core and form an undifferentiated core. Consequently, the radial distribution can be approximated as a single Gaussian and LET/2 in Eq. (4) is replaced by LET_{el} for recoil ions. For recoil ions, r_B becomes less than the interatomic distance a; in which case, a is taken as r_c. The excitation density can be so high that the estimated number density of ionization n_i can exceed the number density n_0 of AgBr. When this should occur, the redistribution of energy and the expansion of the core may take place, r_c is determined so that n_i does not exceed n_0. The maximum local dose D_{max} is set to be $n_i \cdot W = 2.08\times10^{22}\,\mathrm{cm}^{-3}\times5.8\,\mathrm{eV} = 1.20\times10^{17}\mathrm{MeV/cm}^3$.

D. Very heavy recoil ions in α decay

In α decay, the daughter nuclei, such as Pb and Tl, are recoiled with an energy of 100–170 keV. The very heavy recoil ions in α decay produce WIMP-like signals in the detector media, and their contribution to the background signal can be serious. It is important to know what signal will be produced. Lindhard *et al.* [35] introduced a power law approximation for q_{nc} for $Z_1 \neq Z_2$ at very low energies. The model has been applied to binary gases, and satisfactory results were achieved, except in hydrocarbons [21]. We have

$$E_\eta = 0.0142E^{3/2} \tag{25}$$

for Pb ions in Kr (AgBr).

E. Compounds

The chemical composition of a nuclear emulsion is complex and the structure is also not homogeneous. We assume that only the energy deposited on the AgBr crystal is used for the image production, and no energy is transferred from gelatin to the AgBr crystal. The composition (the ratio of number densities) of nuclear emulsion is assumed to be Ag:Br:C(N, O) = 0.4:0.4:2. Light elements such as C, N, and O are regarded as C. H is excluded from the stopping calculation, except for the density calculation. The densities are taken as 6.473 and 3.2 g/cm^3, for the AgBr crystal and fine-grain nuclear emulsion, respectively. The stopping powers S_e and S_n for slow ions are obtained using Eqs. (14) and (15), respectively, unless mentioned otherwise. The stopping power S_c in compounds is obtained using the Bragg-Kleeman rule [41],

$$\frac{S_c}{N_c} = \sum_i \frac{w_i S_i}{N_i}, \tag{26}$$

where N_c is the density of atoms for the compound. S_i, N_i, and w_i are the stopping power, number density, and atom fraction, respectively, of the ith element in the target medium.

The evaluation of q_{nc} for $Z_1 \neq Z_2$ is difficult. Ag and Br recoil ions are produced in the AgBr crystal. For further simplicity, heavy elements, Ag and Br are regarded as Kr to obtain the q_{nc} values in AgBr crystal, because their Z and A values are close to those of Kr. Light ions such as C, N, and O ions, on the other hand, are produced in gelatin and may reach the AgBr crystal. As the Z and A values of these light ions are much smaller than those of Ag and Br atoms, it cannot be assumed that the projectile and the target are the same. A different approach is necessary. The electronic-to-total stopping power ratio S_e/S_T for C ions in C differs less than 5% from that for C ions in Br for $E \geq 20$ keV. Therefore, except for extremely low energies, it may be safe to take the q_{nc} values for C ions in C instead of those for C ions in nuclear emulsion. The value of η for C ions in C was obtained by Eq. (21) with $k = 0.127$. It should be regarded as an upper limit since it over estimates the contributions of secondary ions to q_{nc}. For protons, $q_{nc} = 1$ is adopted in a first approximation.

IV. RESULTS AND DISCUSSION

A. Stopping powers and electronic LET

The Lindhard factor, q_{nc}, for 5–200 keV C ions in C and 5–300 keV Kr ions in Kr is shown in Fig. 2. The values for C ions in C and Kr ions in Kr increase rapidly at low energies and tend to saturate as the energy increases. The stopping powers and $\mathrm{LET_{el}}$ for C and Kr ions in the nuclear emulsion as a function of energy are shown in Figs. 3 and 4. The S_e and $\mathrm{LET_{el}}$ values differ considerably in the low-energy region, where S_n is larger than S_e. $\mathrm{LET_{el}}$ approaches S_e for C ions above ~50 keV. Because $S_e < \mathrm{LET_{el}} < S_T$, and the most contribution to S_T comes from S_e, the approximation of considering C ions in nuclear emulsion as C ions in C for estimating q_{nc} is valid. The S_e and $\mathrm{LET_{el}}$ values for Kr ions in emulsion are different in the low-energy region and continue to differ even at 600 keV.

The mean hit density $(n_F - 1)/R$, where n_F is the number of the filaments, reported for α particles, relativistic 290 MeV/n Be, B, and C ions, and low-velocity Kr ions in a fine-grain nuclear emulsion reported are shown as a function of LET in Fig. 5 (taken from Fig. 4 in Ref. [17]). The grain size is 40 nm. Figure 5 depicts the importance of $\mathrm{LET_{el}}$. The electronic stopping power [32] at the incident energy is employed for Kr ions (closed triangle) [17]. The points for α particles and relativistic ions are in a straight line (broken line) in a log-log plot. In contrast, the data for Kr ions is almost constant and do not stay on the line. The electronic stopping power for 200, 400, and 600 keV Kr ions changes about a factor ~2.5. However, the hit density is within the experimental error. The points for Kr ions are replotted at $\langle \mathrm{LET_{el}} \rangle$ in Fig. 5. The points approach the straight line, when the difference in the developer used is considered (solid line). The $\langle \mathrm{LET_{el}} \rangle$ for Kr ions differ less than 25%.

The stopping power describes how the incident ion losses its energy and does not consider secondary effects. However, LET describes the energy deposited on the target material. The energy deposition attributed to the secondary particles is included in $\mathrm{LET_{el}}$.

B. Track structure

For the directional detection of WIMPs, the LET dependence of hit density is insufficient. The initial radial distributions of local dose for various ions in AgBr crystal are estimated and compared in Fig. 6 for further studies. The averaged value was adopted for LET as in Fig. 5 and the initial energy was taken for r_c and r_p, following custom [29,30]. The r_c and r_p values were calculated for the AgBr crystal. The range of δ rays for fast ions is larger than the grain size. However, to obtain r_p values, the range of δ rays in the AgBr crystal was used rather than in the nuclear emulsion. This is because the r_c/r_p ratio determines the core/penumbra ratio and, consequently, the core density. The core radius is smaller than the grain size. The core density is more

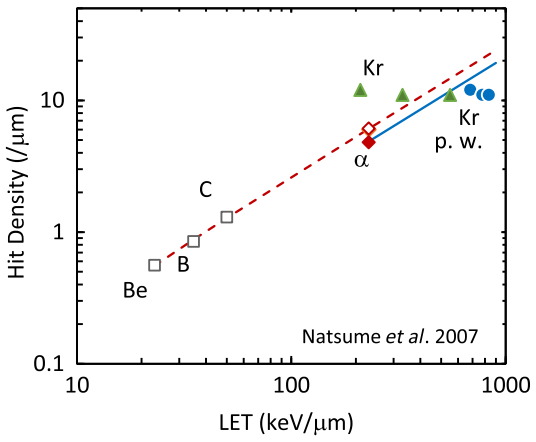

FIG. 5. The mean hit density measured for 5.3 MeV α particles, 290 MeV/n Be, B, and C ions, and 200, 400, and 600 keV Kr ions in fine-grain nuclear emulsion as a function of LET (Fig. 4 in Ref. [17]). The electronic stopping power at incident energy was used for Kr ions (green triangle) [17]. Circles for Kr are replotted at averaged $\mathrm{LET_{el}}$ (blue circle; present work, see the text). Open and closed symbols show the difference in the process with the standard developer and the fine-grain developer, respectively.

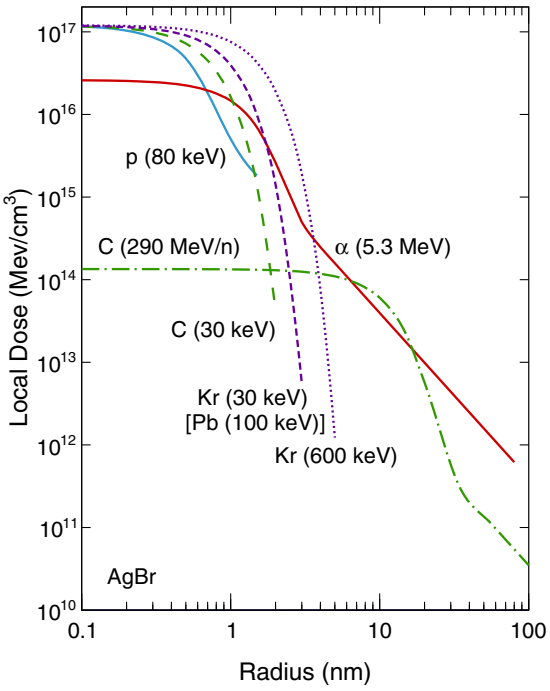

FIG. 6. Initial radial distribution of dose in AgBr crystal for various ions showing the core and penumbra of the heavy-ion track structure. A part of penumbra is shown for 290 MeV/n C ions. The radial distributions for 290 MeV/n Be and B ions are the same as that for C ions when difference in LET is considered. Therefore, the distribution of the Be and B ions are not shown. The curves for slow C and Kr ions have only an undifferentiated core. The initial radial distribution for 100 keV Pb is practically the same as that for 30 keV Kr ions.

important than that in the penumbra in understanding the response of the nuclear emulsion for WIMP searches. The values for r_p was obtained by dividing the range (in g/cm^2) for the maximum δ-ray energy $E_\delta^{\max}$ in nuclear emulsion [42] by the density for AgBr for $E_\delta^{\max} > 10$ keV. At low energies, the extrapolated ranges obtained using the "best-fit" expressions, Eq. (13), by Iskef *et al.* [34] were employed.

The penumbra dose decreases as r^{-2} at large r; however, this is the averaged value. The penumbra consists of δ rays, therefore, the local LET should be regarded as that of δ rays. The dose in the core for relativistic ions is more than two orders of magnitude lower than that for α particles. However, low LET core is inhomogeneous and sparse, and blob formation has to be considered [28].

The track of slow recoil ions consists only of an undifferentiated core. The core radius depends only on $\mathrm{LET_{el}}$ for slow recoil ions when core expansion is taken. Most of energy is deposited within the radius of the grain size as can be seen in Fig. 6. Therefore, it is likely to stay within the grain if it recoils within the grain.

α particles may be used to deduce the response of the detector media to recoil ions when a neutron beam is not easily available. Therefore, it is worthwhile to compare and discuss the tracks of α particles and recoil ions. The energy of Ag and Br recoil ions, which the directional searches target, are generally higher than those for nondirectional searches. The $\mathrm{LET_{el}}$ for recoil ions are considerably larger than those for α particles as shown in Fig. 5. Moreover, the core density calculated for recoil ions is considerably higher than that calculated for α particles in AgBr crystal as shown in Fig. 6. Owing to the band structure, E_1 (E_g) and W for AgBr crystal are significantly smaller than those for atoms and molecules without a band structure, resulting in relatively longer r_B values and less-dense cores for α particles. The core radius r_c of Ag and Br recoil ions and α particles are similar in magnitude due to the expansion of the core. However, the local dose at the center of the core for recoil ions is approximately five times that for α particles. The effects of the difference in the LET and local dose are to be investigated.

Head-tail detection strongly depends on the grain size. Only a few grains are included in a track for Ag or Br ions, which are ones of the main target of fine-grain nuclear emulsions for detecting WIMP. The track for light ions may contain several grains; however, it is doubtful whether a sufficient tone can be achieved. Therefore, this paper does not focus on the head-tail detection. However, an estimation can be achieved by obtaining the Bragg-like curve, $-\mathrm{d}E_\eta/\mathrm{d}R_{\mathrm{prj}}$, where R_{prj} is the projected range, as presented in Ref. [21], with the additional consideration on transversal spreads.

C. Background

The very heavy recoil ions in α decay may produce WIMP-like tracks, as mentioned in Sec. III D. The q_{nc} values estimated for 100–180 keV Pb ions in AgBr crystal are shown in Fig. 2. The $\langle \mathrm{LET_{el}} \rangle$ value calculated for the recoil ions and Pb ions are considerably close (Table I). In fact, the $\langle \mathrm{LET_{el}} \rangle$ values for 100 and 170 keV Pb ions are 360 and 540 keV/μm, respectively, and those for 30 and 100 keV Kr ions are 340 and 550 keV/μm, respectively. The initial radial distributions for 30 keV Kr ions and 100 keV Pb ions are practically the same in Fig. 6. Generally, one does not observe the heavy recoil ions and α particles as separate particles because they are produced simultaneously. The Pb track is associated with a considerably larger α-particle track. However, in some cases, Pb recoiled at the boundary of the AgBr crystal and gelatin such that an α particle enters the gelatin or escapes from the nuclear emulsion, and the Pb recoil fully goes into the AgBr crystal. Then, the recoil Pb ion can produce a WIMP-like signal.

Search for dark matter requires large exposure, i.e., mass × time; therefore, to obtain a good signal-to-noise ratio, causes of noises must be eliminated as much as possible by adjusting the sensitivity of nuclear emulsion. Major contributions to the background in underground laboratories are γ rays and neutrons. Since LET for the electron is much smaller than $\mathrm{LET_{el}}$ for recoil ions, γ rays can be ignored by adjusting the sensitivity of nuclear emulsion and/or using the cryogenic crystal effect [43]. Neutrons can produce WIMP-like signals as neutron scattering is used to produce recoil ions to mock dark matter signal in the detector media [18]. These signals are distinguished using daily modulation based on directionality measurements. At WIMP search, the nuclear emulsion is planned to be constructed on an equatorial mount. The position and direction will provide some insights on reject the very heavy recoil ions in α decay as well as γ rays and neutrons.

Special caution should be paid to the knock-on protons produced by fast neutrons [44] that recoil the hydrogen in the gelatin of nuclear emulsion, as used in film badges, which produce latent image in an AgBr crystal. The mass fraction of hydrogen in the nuclear emulsion is only ∼1.6%; however, the number fraction amounts to ∼40% and cannot be disregarded in considering effects of background neutrons. The result for 5.3 MeV α particles shown in Fig. 6 can also be interpreted as the result for ∼1.3 MeV protons, although the LET value differs. The difference in LET can be addressed simply, since the Bethe formula for stopping power for fast ions scales as Z_1^2, a quarter LET for α particles will yield the distribution for ∼1.3 MeV protons. Fast protons may be disregarded by the range. However, for directional detection, at least two or three grains are necessary (size 100–200 nm). With conventional optical reading system, the submicron track length is essential. Protons with energies less than ∼50 keV become difficult to distinguish from WIMP signals based on the range alone. The energy of the Bragg peak for protons in AgBr crystal is approximately 80 keV. The range for

80 keV protons is 0.74 μm. The r_c values obtained using the Bohr criterion, becomes smaller than a for protons with energy of ~70 keV; thus $r_c = a = 0.288$ nm is regarded as the minimum core radius. The results for 80 keV protons show a dose distribution of almost the minimum radius. The maximum local dose calculated for 80 keV protons using $r_c = 0.3$ nm exceeds D_{max}; therefore, the core expansion, $r_{ex} = 0.46$ nm, was adopted. The initial radial distribution of the dose in AgBr crystal attributed to 80 keV protons is shown in Fig. 6. The local dose of the penumbra attributed to δ rays ($r > r_{ex}$) was obtained using Eq. (6) with $r_c = 0.3$ nm and $r_p = 1.5$ nm. The local dose of the penumbra may not play an important role in the case of low-energy protons. This holds if the track consists of only an undifferentiated core with $r_{ex} = 0.54$ nm. An undifferentiated core with $r_{ex} = 0.48$ nm was adopted for 25 keV protons in Table I.

D. General remarks

The errors in the q_{nc} values may be 5%–15% in the Lindhard model, as discussed in Ref. [20]. We adopt $k = 0.15$ instead of $k = 0.158$ for Kr ions in Kr. This simplification may underestimate the η value by approximately 4%. The errors in the independent element approximation for C in AgBr may be 10%–20%. The overall uncertainties in the present calculation may be larger. However, the latent image production mechanism is complicated and quantitative prediction is difficult because the sensitivity of nuclear emulsion depends on many factors. The relative values of q_{nc}, LET_{el}, and the track parameters are utilized, and the errors in the relative values are considerably low.

It is important to know whether the latent image formation is determined by LET (or energy per crystal) or local dose (local deposited-energy density). The $\langle \mathrm{LET} \rangle$ for protons are about 100 keV/μm and are considerably smaller than $\langle \mathrm{LET}_{el} \rangle$ for Kr recoil ions and 1/3 that for C recoil ions in a submicron range. If LET is the main factor, then it may not be difficult to disregard protons from Kr recoil ions. It may be more difficult for C recoils, although, it may still be possible to reject protons. However, the maximum local dose for protons is the same as those for C and Kr recoil ions. It may be naive to assume that the grain becomes developable when the local dose shown in Fig. 6 exceeds a particular threshold value and the dose above this threshold will contribute the latent image production and determine the sensitivity. The reaction kinetics may have to be considered [22,31].

The fraction of the energy contribute to the electronic excitation by the primary ion can be expressed as

$$\frac{E_\eta^{pr}}{E_\eta} = \frac{\int_0^R S_e \mathrm{d}x}{q_{nc} E} = \frac{\int_0^R (-\mathrm{d}E/\mathrm{d}x)_e \mathrm{d}x}{\int_0^R \mathrm{LET}_{el} \mathrm{d}x}, \tag{27}$$

where E_η^{pr} is the electronic energy given directly by the primary ion. For C ions, the fraction due to secondary recoils can be ignored in the present simple model. However, for Ag and Br recoil ions, the fraction due to secondaries can be comparable to that attributed to the primary ions at low energies (Fig. 4). The radial distribution of the dose presented in Fig. 6 is that of the initial condition. The radial distribution will expand rapidly, and the secondary tracks will be included in it as the reaction kinetics proceeds. There may be a few energetic secondary recoils outside the expansion radius.

The nuclear stopping process recoils Ag and Br atoms in the crystal, and the replacement of atoms may cause the distortion of crystal. The effect was not treated herein, it has to be considered. The energy spent as heat may increase the local temperature of the crystal and influence the latent image formation. The energy ν converted into thermal energy. The thermal energy produces phonon and can be used [43]. The nuclear LET (LET_{nc}), the energy given to nuclear motion in the stopping process per unit path length, is expressed as

$$\begin{aligned} \mathrm{LET}_{nc} &= -\frac{\mathrm{d}E_\nu}{\mathrm{d}x} = -\frac{\mathrm{d}E_\nu}{\mathrm{d}E}\frac{\mathrm{d}E}{\mathrm{d}x} = \frac{\mathrm{d}E_\nu}{\mathrm{d}E} S_T, \\ &\approx \frac{\Delta E_\nu}{\Delta E} S_T. \end{aligned} \tag{28}$$

However, some parts of η contributes to the thermal energy. Some parts of η are used for light emission [45], while other parts are spent as chemical reactions; the remaining is spent as heat in nuclear emulsion.

The present model is simple, and its assumptions are clear. One can refine the calculation or extend the model when needed. The microscopic track structure obtained herein does not immediately predict the latent image in nuclear emulsion owing to the complexity of the response of nuclear emulsion to ionizing radiation. The present results are utilized to adjust the sensitivity and grain size, determine the optimum developing conditions, etc. The track deviates and has branches. These effects have to be considered in detail. The spacial distribution for a single event may appear to be considerably different from that averaged over many events. It is difficult to obtain the character of the track owing to a single event using simulations.

This study focuses on the sensitivity of nuclear emulsions as WIMP detectors. It is beyond the scope of the present work to provide prospects for directionality in WIMP detectors. For overall performance of nuclear emulsions as WIMP detectors, refer to the literature [46–50]. It is crucial to preserve the initial direction of the recoiling nucleus. The initial direction of the first recoiling nucleus may be obtained via conventional WIMP-atom elastic collision kinematics. The recoiled nucleus undergoes continuous collisions with the target atoms. Slow ions experience a considerable deviation from the initial trajectory because of scattering. We present a short discussion on the

estimation of multiple scattering angles in the Appendix. Detailed Monte Carlo simulations, such as those in the TRIM package, can be useful tools for obtaining the spatial profile of energy deposition, q_{nc} values, etc., provided that the elementary processes are well known.

V. SUMMARY

The electronic energy deposition caused by slow C and Kr ions in nuclear emulsion was estimated for the directional detection of dark matter (WIMPs). Electronic LET was introduced, and its importance in explaining the mean hit density for slow Kr ions, α particles, and relativistic heavy ions was demonstrated. The so-called core and penumbra of heavy-ion track structure was considered and modified for various ions. The initial radial distributions of electronic dose for various ions were presented and compared for further research. The tracks attributed to the very heavy recoil ions (100–180 keV Pb ions) produced in α decay were also estimated. Furthermore, the track for protons was examined to evaluate the influence of neutrons, which is one of main background sources. Some backgrounds are difficult to distinguish with WIMP signals using the difference in LET or track structure, in such cases, directional detection becomes important. A brief discussion on angular scattering is provided in the Appendix.

ACKNOWLEDGMENTS

We would like to thank Dr. T. Naka for guiding us on these topics, facilitating variable discussions, and providing information on nuclear emulsions. We are grateful to Professor T. Tani for reading an early version of the manuscript and providing helpful comments. The work described herein was supported in part by the Office of Basic Energy Science of the Department of Energy. This is Document No. NDRL 5242 from the Notre Dame Radiation Laboratory. This work was supported by KAKENHI Grant-in-Aids (Grant No. 18K13567). The manuscript English was edited by enago [51].

APPENDIX: ANGULAR SCATTERING

The angular scattering of slow ions is predominantly attributed to the momentum transfer of the ion to the target atom [37,39]. The standard theory of multiple scattering with small-angle approximation was constructed by Meyer [52] for the Thomas-Fermi (TF) interaction and, by Sigmund and Winterbon [53] for the TF and Lenz-Jensen (LJ) interactions. The results are expressed in terms of the reduced scattering angle ϑ and the reduced thickness of the scattering layer τ. Valdés and Arista used the potential proposed by Zieglar, Biersack, and Littmark [54]. The half width for the angular distributions for the three interactions is practically the same for large τ values ($\tau \gtrsim 2$). There is a considerable difference between the TF and LJ predications at small τ values. The values for the Zieglar, Biersack, and Littmark potential lie between the two. The experimental results also lie between the TF and LJ interaction curves at the small τ [55]. The half width for the reduced scattering angle $\vartheta_{1/2}$ for the TF and LJ interactions is constructed from the tables for the angular distribution in the literature [53] by interpolation. The following expressions are obtained for the middle values of the TF and LJ interactions.

$$\vartheta_{1/2} = 0.03444\tau^4 - 0.1497\tau^3 + 0.1883\tau^2 + 0.2259\tau - 0.0091, \qquad 0.1 \le \tau \le 2, \tag{A1}$$

$$\vartheta_{1/2} = -1.055\times10^{-5}\tau^4 + 6.019\times10^{-4}\tau^3 - 0.01419\tau^2 + 0.2819\tau + 0.03494, \quad 2 \le \tau \le 20. \tag{A2}$$

The scattering angle is a function of the thickness. The range R is considered a measure, and simple expressions for the reduced (dimensionless) range ρ [56] is expressed as

$$\rho = 1.53\varepsilon^{2/3}, \qquad \varepsilon \le 0.2, \tag{A3}$$

$$\rho = 3.06\varepsilon, \qquad 0.08 \le \varepsilon, \tag{A4}$$

which affords values within 20% for TF without energy loss to electrons for $\varepsilon \le 2$. The larger of the two may be adopted in the vicinity of $\varepsilon \approx 0.1$. The ranges measured along the track R and the projected range R_{prj} are approximately related as [37]

$$R/R_{prj} \cong 1 + \frac{1}{3}\frac{A_2}{A_1}. \tag{A5}$$

The reduced scattering angle ϑ, the reduced range ρ, and reduced thickness τ are converted into absolute terms:

$$\vartheta = \theta\frac{\varepsilon}{2}\frac{A_1 + A_2}{A_2}, \tag{A6}$$

$$\tau = \frac{a_s^2}{r_s^2}n_c = \pi a_s^2 N x, \tag{A7}$$

$$\rho = RN \cdot 4\pi a_s^2 \frac{A_1 A_2}{(A_1 + A_2)^2}, \tag{A8}$$

where a_s is the screening radius [Eq. (18)], $r_s \approx N^{-1/3}/2$ is half the distance of the immediate neighboring atoms, and $n_c = \pi r_s^2 N x$ is the number of collisions. The reduced energy ε is given by Eq. (19).

The above-discussed theories are for a thin target, and it is assumed that the energy loss of an ion is small compared to its initial energy. This is not the case for directional dark matter searches. Valdés and Arista [54] discussed the effect of finite-energy loss on multiple-scattering angular distributions. The energy-loss effect to the angular half width in

the case of slow ions may be represented when the mean energy defined in the following form is used:

$$\varepsilon_m = \frac{1}{4}\varepsilon_0(1+\mu^{1/2})^2, \qquad 0.3 \le \mu \le 1, \qquad \text{(A9)}$$

where ε_0 and $\varepsilon_1 = \mu\varepsilon_0$ are the initial and final energies, respectively. The relation also holds in the case of absolute terms, E_0 and $E_1 = \mu E_0$. Equation (A9) holds for the energy-loss parameter $(1-\mu)$ ranging from 0 to 0.7. The mean energy ε_m is used when the reduced half width $\vartheta_{1/2}$ obtained using Eqs. (A1) or (A2) is converted into absolute term $\theta_{1/2}$ using Eq. (A6).

The tracks of the range above 100 nm are considered for the directional search in the nuclear emulsion. We estimate $\theta_{1/2}$ for C (N, O) ions with the energy of 35 keV and Kr (Br, Ag) ions with the energy of 200 keV in the nuclear emulsion. We apply a simple approximation for a compound target. In the calculations of ε and a_0, a compound is approximated using a monoatomic target with the same density and average Z and A values. The Z and A are taken to be 11.5 and 25, respectively, in the nuclear emulsion. The ε and k values are 3.9 and 0.19, respectively, for C ions with the energy of 35 keV and 0.9 and 0.11, respectively, for Kr ions with the energy of 200 keV. The results are shown in Fig. 7. The solid curve is the middle value of the Thomas-Fermi and Lentz-Jensen interactions, $(\mathrm{TF}+\mathrm{LJ})/2$. The half width $(\theta_{1/2})$ increases with x. The correction for the target thickness, the energy-loss effect, exhibits upward deviation from the $(\mathrm{TF}+\mathrm{LJ})/2$ curve. The deviation increases considerably for $x/R_{\mathrm{prj}} \gtrsim 0.3$. The produced ionization induces the bell-shaped contour based on the above-discussed theories. However, the longitudinal straggling induces the drop-shaped contour, as shown in the theory [56] and experiments [57]. The range obtained by Eqs. (A3) or (A4) is basically longer than real values because the equations do not consider the electronic stopping power. Therefore, it is not reasonable to consider the $\theta_{1/2}$ value at $x = R_{\mathrm{prj}}$.

NEWSdm collaboration [48] calculated for the angular deviation for nuclear recoils in emulsion using the TRIM simulation package [32]. The definition of the angle is different from the present one but not too different. The results reported by NEWSdm are shown in Fig. 7. The width σ_θ is converted into $\theta_{1/2}$ as $\theta_{1/2} = 2.35\sigma_\theta/2$. The horizontal positions are arbitrary. The agreements of the present calculations with the energy-loss effect are

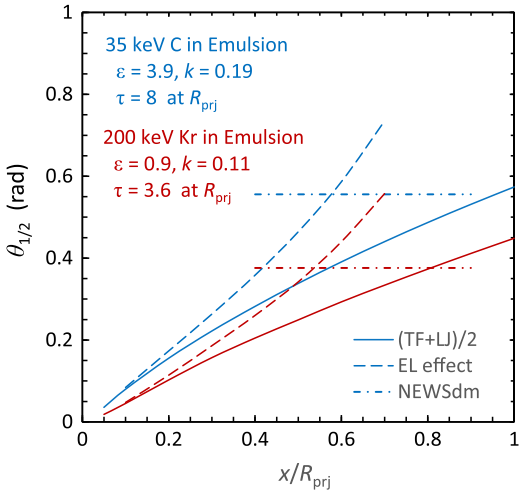

FIG. 7. Half width of the angular distribution $\theta_{1/2}$ for 35 keV C ions and 200 keV Kr ions in nuclear emulsion as a function of the thickness x in unit of the projected range R_{prj}. The solid curves indicate the middle value of the Thomas-Fermi and Lentz-Jensen, $(\mathrm{TF}+\mathrm{LJ})/2$ interactions; the dashed curves show the inclusion of the energy-loss effect [54]. The dotted-dash lines represent the calculations obtained by NEWSdm [48] using the TRIM simulation package (refer to the text).

obtained at $x/R_{\mathrm{prj}} = 0.5$–0.6. Lindhard *et al.* [58] estimated the ρ values for TF with and without electronic stopping power for various k values as a function of ε. The ratio of ρ obtained with and without [Eq. (A4)] electronic stopping power are ~0.6 and ~0.7 for C recoils with the energy of 35 keV and Kr recoils with the energy of 200 keV, respectively, in the nuclear emulsion. The longitudinal straggling may reduce the scattering angle. Furthermore, the ionization decreases with q_{nc} as the recoils decelerate toward the end of the track. Therefore, x/R_{prj} value of 0.5–0.6 may be considered reasonable. This yields a practical measure for use in the present calculation. The details of the calculation and application for other directional detector materials will be published elsewhere.

The present method is convenient for obtaining the relative values, general trends, and energy dependence to compare targets with various kind and compositions. The Monte Carlo simulation should be used when accurate values are needed. It affords the ensemble average for many tracks and may be used for statistical analysis. The shape of each track can be considerably different from the averaged one, as shown in the figures in Refs. [49,57,59].

[1] F. Zwicky, Helv. Phys. Acta **6**, 110 (1933).
[2] V. C. Rubin and J. W. K. Ford, Astrophys. J. **159**, 379 (1970).
[3] V. C. Rubin, J. W. K. Ford, and N. Thonnard, Astrophys. J. **238**, 471 (1980).
[4] T. A. McKay *et al.*, Astrophys. J. Lett. **571**, L85 (2002).
[5] D. Clowe, M. Bradač, A. H. Gonzalez, M. Markevitch, S. W. Randall, C. Jones, and D. Zaritsky, Astrophys. J. Lett. **648**, L109 (2006).
[6] R. Massey, T. Kitching, and J. Richard, Rep. Prog. Phys. **73**, 086901 (2010).
[7] M. W. Goodman and E. Witten, Phys. Rev. D **31**, 3059 (1985).
[8] J. Ellis and R. A. Flores, Phys. Lett. B **263**, 259 (1991).
[9] J. D. Lewin and P. F. Smith, Astropart. Phys. **6**, 87 (1996).
[10] S. Suzuki and A. Hitachi, Application of rare gas liquids to radiation detectors, in *Charged Particle and Photon Interactions with Matter: Recent Advances, applications, and Interfaces*, edited by Y. Hatano *et al.* (Taylor and Francis, Boca Raton, 2010), Chap. 31.
[11] N. J. C. Spooner, J. Phys. Soc. Jpn. **76**, 111016 (2007).
[12] E. Aprile *et al.* (XENON Collaboration), Phys. Rev. Lett. **121**, 111302 (2018).
[13] C. Amole *et al.* (PICO Collaboration), Phys. Rev. Lett. **118**, 251301 (2017).
[14] R. Agnese *et al.* (SuperCDMS Collaboration), Phys. Rev. D **97**, 022002 (2018).
[15] D. N. Spergel, Phys. Rev. D **37**, 1353 (1988).
[16] J. R. Erskine, Nucl. Instrum. Methods **162**, 371 (1979).
[17] M. Natsume, K. Hoshino, K. Kuwabara, M. Nakamura, T. Nakano, K. Niwa, O. Sato, T. Tani, and T. Toshito, Nucl. Instrum. Methods Phys. Res., Sect. A **575**, 439 (2007).
[18] T. Naka *et al.*, Nucl. Instrum. Methods Phys. Res., Sect. A **718**, 519 (2013).
[19] N. D'Ambrosio *et al.*, J. Instrum. **9**, C01043 (2014).
[20] A. Hitachi, Astropart. Phys. **24**, 247 (2005).
[21] A. Hitachi, Radiat. Phys. Chem. **77**, 1311 (2008).
[22] A. Hitachi, Instruments **5**, 5 (2021).
[23] N. J. Carrera and F. C. Brown, Phys. Rev. B **4**, 3651 (1971).
[24] A. Testa, W. Czaja, A. Quattropani, and P. Schwendimann, J. Phys. C **21**, 2189 (1988).
[25] K. A. Yamakawa, Phys. Rev. **82**, 522 (1951).
[26] R. Katz and F. E. Pinkerton, Nucl. Instrum. Methods **130**, 105 (1975).
[27] M. P. R. Waligórski, R. N. Hamm, and R. Katz, Int. J. Radiat. Appl. Instrument. D: Nucl. Tracks Radiat. Meas. **11**, 309 (1986).
[28] A. Mozumder, *Fundamentals of Radiation Chemistry* (Academic Press, San Diego, 1999).
[29] A. Chatterjee and H. J. Shaefer, Radiat. Environ. Biophys. **13**, 215 (1976).
[30] J. L. Magee and A. Chatterjee, J. Phys. Chem. **84**, 3529 (1980).
[31] A. Hitachi, T. Doke, and A. Mozumder, Phys. Rev. B **46**, 11463 (1992).
[32] J. F. Ziegler, M. D. Ziegler, and J. P. Biersack, Nucl. Instrum. Methods Phys. Res., Sect. B **268**, 1818 (2010).
[33] A. Mozumder, J. Chem. Phys. **60**, 1145 (1974); **62**, 4585 (1975).
[34] H. Iskef, J. W. Cunningham, and D. E. Watt, Phys. Med. Biol. **28**, 535 (1983).
[35] J. Lindhard, V. Nielsen, M. Scharff, and P. V. Thomsen, Mat. Fys. Medd. K. Dan. Vidensk. Selsk. **33**, 1 (1963).
[36] J. Lindhard and A. Winther, Mat. Fys. Medd. K. Dan. Vidensk. Selsk. **34**, 1 (1964).
[37] J. Lindhard and M. Scharff, Phys. Rev. **124**, 128 (1961).
[38] J. P. Biersack, Z. Phys. A **211**, 495 (1968).
[39] J. P. Biersack, E. Ernst, A. Monge, and S. Roth, Tables of electronic and nuclear stopping powers and energy straggling for low-energy ions, Hahn-Meitner Institut Publication Report No. HMI-B 175, 1975.
[40] I. S. Tilinin, Nucl. Instrum. Methods Phys. Res., Sect. B **98**, 380 (1995).
[41] G. F. Knoll, *Radiation Detection and Measurement* (John Wiley and Sons, Inc., New York, 2000).
[42] W. N. Barka, *Nuclear Research Emulsions*, 15-I (Academic Press, New York, 1963).
[43] M. Kimura *et al.*, Nucl. Instrum. Methods Phys. Res., Sect. A **845**, 373 (2017).
[44] H. Park, J. Kim, Y. M. Hwang, and K.-O. Choi, Appl. Radiat. Isot. **81**, 302 (2013).
[45] F. Moser and S. Lyu, J. Lumin. **3**, 447 (1971).
[46] A. Aleksandrov *et al.* (NEWS Collaboration), arXiv: 1604.04199.
[47] C. A. J. O'Hare, B. J. Kavanagh, and A. M. Green, Phys. Rev. D **96**, 083011 (2017).
[48] N. Agafonova *et al.* (NEWSdm Collaboration), Eur. Phys. J. C **78**, 578 (2018).
[49] C. Couturier, J. P. Zopounidis, N. Sauzet, F. Naraghi, and D. Santos, J. Cosmol. Astropart. Phys. 01 (2017) 027.
[50] S. E. Vahsen *et al.*, arXiv:2008.12587v2.
[51] www.enago.jp.
[52] L. Meyer, Phys. Status Solidi (b) **44**, 253 (1971).
[53] P. Sigmund and K. B. Winterbon, Nucl. Instrum. Methods **119**, 541 (1974).
[54] J. E. Valdés and N. R. Arista, Phys. Rev. A **49**, 2690 (1994).
[55] G. Sidenius and N. Andersen, Nucl. Instrum. Methods **128**, 271 (1975).
[56] K. B. Winterbon, P. Sigmund, and J. B. Sanders, Mat. Fys. Medd. K. Dan. Vidensk. Selsk. **37**, 1 (1970).
[57] G. E. Evans, P. M. Stier, and C. F. Barnet, Phys. Rev. **90**, 825 (1953).
[58] J. Lindhard, M. Scharff, and H. E. Schiøtt, Mat. Fys. Medd. K. Dan. Vidensk. Selsk. **33**, 1 (1963).
[59] Y. Tao *et al.* (MIMAC Collaboration), Nucl. Instrum. Methods Phys. Res., Sect. A **985**, 164569 (2021).